







Hierarchical maturation of structural brain connectomes from birth to childhood

Received: 19 April 2025

Accepted: 14 January 2026

Published online: 22 January 2026

 Check for updates

Tengda Zhao ^{1,2,3,11}, Minhui Ouyang ^{4,5,11}, Xiao-Jing Shou^{1,2,3,11}, Shanbin Zhang^{1,2,3}, Jiatong Ju^{1,2,3}, Xuhong Liao ⁶, Meizhen Han^{1,2,3}, Lianglong Sun ^{1,2,3}, Xiaoyue Wang⁷, Yunman Xia ^{1,2,3}, Di Hu⁸, Huiying Kang⁸, Jianlin Guo⁸, Qian Wang^{1,2,3}, Maolin Li^{1,2,3}, Ran Huo⁹, Ying Liu⁹, Huishu Yuan⁹, Yun Peng⁸ , Hao Huang ^{4,5}  & Yong He ^{1,2,3,10} 

The postnatal white matter connectome undergoes profound reorganization, yet the topological principles governing its spatiotemporal maturation remain largely unknown. Using connectome mapping, machine learning, and neurobiological annotation, we show hierarchical network development from birth to childhood and its association with neurobiological signatures. We identify two cardinal topological transformations that change rapidly during infancy and continue to refine into childhood, as characterized by nonlinear global increases in network efficiency and robustness to nodal attack, and regional reorganization with accelerated hub consolidation and prolonged modular reconfiguration, predominantly involving the prefrontal and insular cortices. Early developmental trajectories of these association cortices predict late childhood network architecture through local microstructural maturation of connected white matter tracts. These patterns align with well-established multiscale cortical hierarchies, including anatomical, evolutionary, and energy metabolism axes. Our findings reveal critical neurotopological milestones after postnatal development and establish a unified multiscale framework linking macroscale network dynamics to biologically constrained rules.

The human brain undergoes remarkable reorganization during early postnatal development, evolving from a prenatal prototype to a dynamically maturing architecture. This maturation process involves key neurodevelopmental events, such as axonal myelination and synaptic pruning^{1,2}, which are orchestrated through multifaceted neurobiological regulation^{3,4}. These microstructural adaptations drive the maturation of macroscopic white matter (WM) tracts across regions^{5–8}, resulting in the progressive optimization of network

communication within the structural connectome⁹, which supports subsequent functional specialization^{10–13}. Systematic characterization of the maturation of the WM connectome from birth through childhood and elucidation of its neurobiological determinants are critical for understanding the fundamental principles underlying human brain development¹⁴. Here, we present a comprehensive mapping of the hierarchical maturation of the WM connectome from birth to childhood and the associated neurobiological signatures.

¹State Key Laboratory of Cognitive Neuroscience and Learning, Beijing Normal University, Beijing, China. ²Beijing Key Laboratory of Brain Imaging and Connectomics, Beijing Normal University, Beijing, China. ³IDG/McGovern Institute for Brain Research, Beijing Normal University, Beijing, China. ⁴Department of Radiology, Children's Hospital of Philadelphia, Philadelphia, PA, USA. ⁵Department of Radiology, Perelman School of Medicine, University of Pennsylvania, Philadelphia, PA, USA. ⁶School of Systems Science, Beijing Normal University, Beijing, China. ⁷School of Medical Technology, Beijing Institute of Technology, Beijing, China. ⁸Department of Radiology, Beijing Children's Hospital, Capital Medical University, National Center for Children's Health, Beijing, China. ⁹Department of Radiology, Peking University Third Hospital, Beijing, China. ¹⁰Chinese Institute for Brain Research, Beijing, China. ¹¹These authors contributed equally: Tengda Zhao, Minhui Ouyang, Xiao-Jing Shou. ✉e-mail: ppengyun@hotmail.com; huangh6@chop.edu; yong.he@bnu.edu.cn

Histological studies have revealed that the microstructures of the human brain, including synaptic pruning and myelination, exhibit a regionally heterogeneous maturation process between the primary and association cortices during the early years of life^{15–17}. Non-invasive diffusion MRI studies *in vivo* have demonstrated that the WM tracts associated with the sensorimotor cortex mature earlier than those associated with the transmodal cortex^{6,18,19}. These heterogeneous maturation patterns support the emergence of functional specialization: the earlier maturation of the sensorimotor pathway provides reliable environmental input channels that are critical for experience-dependent plasticity²⁰, whereas the prolonged development of frontal WM pathways enables highly complex signal communications that facilitate advanced cognitive abilities^{21,22}. While previous diffusion MRI studies have revealed the maturation of WM pathways from birth to childhood^{7,23,24}, they were limited to local views of specific WM pathways, and a global perspective of maturation processes at the network level is lacking.

Developmental connectomics provides a unique and powerful framework for exploring the maturation of structural WM networks. Within this framework, regional partitions and reconstructed fibre bundles are typically defined as nodes and edges, respectively^{9,25}. Quantitative graph theoretical analyses have revealed prominent wiring patterns within the WM connectome, including an efficient small-world architecture, highly centralized hubs, and distributed module structures, which are largely established in neonates^{26–28}. Heterogeneous development of the network topology continue into childhood, characterized by the increased integration capacity of nodes^{28–32}, consolidated hub enhancements³³, and dynamic reordering of module topologies³⁴ (for reviews, see refs. 9,25,35). Despite these insights, previous studies have focused primarily on discrete developmental phases such as infancy^{28,36}, toddlerhood²⁹ or childhood^{30,37,38}, hindering our understanding of the continuous maturation that occurs during early years of life^{33,39}. Furthermore, emerging evidence suggests that the microstructural maturation of WM tracts, such as axonal elongation and myelination processes, is supported by multiple biological processes, including neurotransmitter activity, metabolism, and genetic regulation^{3,4}. However, the relationship between the development of macroscopic WM networks and the underlying neurobiological and microstructural signatures remains largely unknown.

To address these knowledge gaps, we collected multisite diffusion MRI scans from 221 typically developing children aged 0–8 years. Using graph theoretical approaches, we delineated the typical maturation pattern of the structural connectome during this critical developmental stage. Specifically, we first examined the maturation trajectories of global network efficiency and resilience. Next, we elucidated nodal-level topological reconfiguration by assessing efficiency optimization, hub configurations, and modular flexibility. We then explored associations between regional network maturation and neurobiological hierarchies spanning anatomical features, molecular/evolutionary signatures, functional/metabolic profiles, and WM microstructures. Finally, using two independent datasets with longitudinal brain scans^{40,41}, we replicated our main findings derived from cross-sectional data. Our results reveal previously unrecognized hierarchical principles of structural connectome maturation during the early years of life and how hierarchical network reorganization occurs via biologically constrained developmental processes.

Results

After rigorous quality control, the final analytical sample encompassed: (i) a Discovery Dataset of 221 typically developing children aggregated from two sites, Subset 1 ($n = 114$, aged 0.17–7.91 years) and Subset 2 ($n = 107$, aged 0.58–7.1 years); and (ii) a Replication Dataset comprising two longitudinal validation subsets, the Baby Connectome Project (BCP) cohort with 170 infant scans (0–2.5 years) and the EBDS-2 cohort including 97 children (0–6 years) scanned at five discrete time points (0, 1, 2, 4, and 6 years). For details, see “Methods”.

Global maturation of network efficiency and resilience in the structural connectome

We first established individualized structural WM connectomes of the brain using node-edge definition protocols (Discovery Dataset, Fig. 1A). Here, network nodes were obtained by parcellating cortical grey matter into 500 uniform regions⁴², and network edges were obtained by quantifying interregional connectivity via tractography-derived streamline counts²⁸. To characterize the developmental trajectory of the brain network topology from birth to childhood (0–8 years), we performed a multi-model comparison of linear and saturating exponential increases using Akaike’s information criterion (AIC)

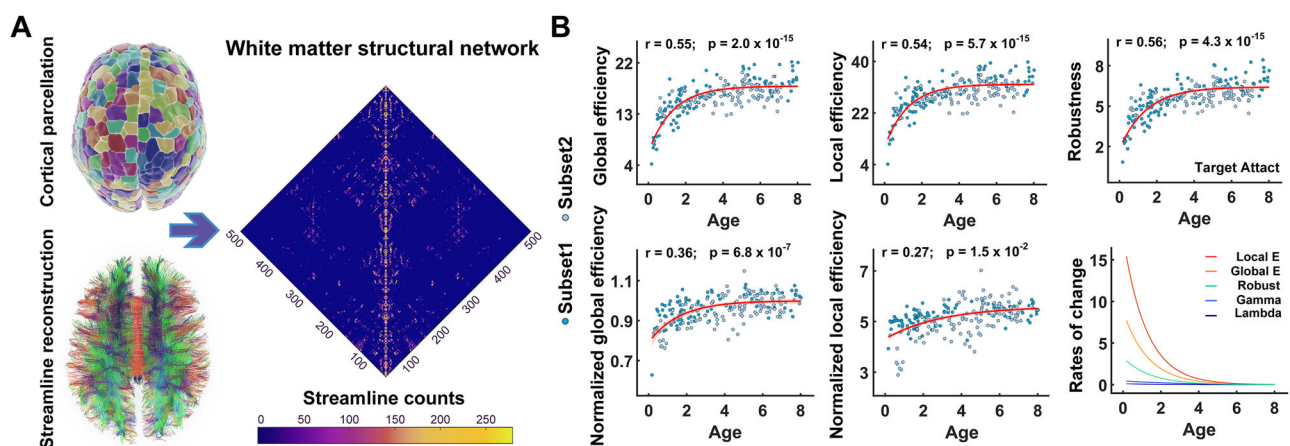


Fig. 1 | The construction of the brain structural network and the global topological changes from birth to childhood. A Construction of the individual structural connectomes. Network nodes were obtained by parcellating individual cortical grey matter into 500 regions on the basis of T1-weighted images, and network edges were obtained via diffusion MRI-based deterministic tractography in the native space. **B** Significant age-related increases (uncorrected p , two-tailed) were observed for global/local efficiency, normalized global/local efficiency and

network robustness with targeted attack results serving as an illustrative example. The scatter plot shows the fitting curves with the shaded area indicating the 95% confidence interval around the fitted mean. Dark blue and light blue dots indicate individuals from the Subset 1 and Subset 2 of the Discovery Dataset, respectively. Large rates of change in local efficiency, global efficiency, and robustness at the infancy stage were identified (last panel). Source data are provided as a Source Data file.

weights to select the appropriate model⁴³. Notably, network sparsity and brain size were included as covariates to ensure that the age-related changes in network topology were not simply driven by the number of network edges or increases of brain volume. Site effects were controlled for by including site label as a random effect in the statistical models.

Quantitative global network analysis revealed nonlinear developmental patterns in both global efficiency (E_{glob}) and local efficiency (E_{loc}). Both metrics exhibited saturating exponential increases with age (E_{glob} : $r = 0.55$, $p = 2.0 \times 10^{-15}$; E_{loc} : $r = 0.54$, $p = 5.7 \times 10^{-15}$) (Fig. 1B). We further assessed the normalized global efficiency (λ) and normalized local efficiency (γ), which measure the ratio between the efficiency of the actual network and the mean efficiency of 100 matched random networks preserving sparsity and degree distribution^{44,45}. These metrics were subsequently combined into a composite measure of small-worldness⁴⁶, $\sigma = \gamma/\lambda$. A value greater than 1 indicates a small-world network, representing an optimized balance between information integration and segregation⁴⁷. Although the structural connectomes of all children exhibited prominent small-world architectures ($\sigma = 5.23 \pm 1.18$, range: 3.5–8.5), we observed significantly saturating exponential increases in normalized global efficiency and normalized local efficiency (λ : $r = 0.36$, $p = 6.8 \times 10^{-7}$; γ : $r = 0.27$, $p = 0.015$) (Fig. 1B), and a marginal increase in σ ($r = 0.02$, $p = 0.13$). Given the known neurodevelopmental vulnerability of hub regions²⁵, we quantified global network robustness, through targeted hub attacks and random failure simulations^{48,49}. Specifically, we assessed how the size of the largest connected component (LCC) of the network changed as nodes were progressively removed, either by descending nodal strength (targeted attack) or at random (random failures). Network robustness was quantified as the area under the LCC–node removal curve. We found that network robustness against both hub and random attacks increased nonlinearly with age (targeted: $r = 0.56$, $p = 4.3 \times 10^{-15}$; random: $r = 0.55$, $p = 3.0 \times 10^{-15}$) (Fig. 1B). Analyses on the rates of change in global network metrics revealed critical increases which predominantly occur during infancy and continuing into childhood (e.g., global efficiency: the rate of change reduced into 1/9 of the max after the age of 3.5 years) (Fig. 1B, last panel). These results highlight a globally accelerated maturation of the structural connectome, with topological optimization occurring during early postnatal development.

Heterogenous maturation in communication efficiency between primary and transmodal association cortices

The regional efficiency of each node, which represents its communication capacity across the entire WM connectome, was then measured. We observed two distinct growth patterns in the communication efficiency of brain nodes: linear increases mainly in the primary sensorimotor cortex, and saturating exponential increases mainly in frontal and temporal cortices and the insular cortex (False Discovery Rate (FDR) corrected $q < 0.05$, corresponding to uncorrected $p = 0.008$) (Fig. 2A). Representative fitting curves for these two patterns are shown (Fig. 2A). Next, we tested whether the spatial distribution of this maturation pattern was circumscribed by general brain organizations. We classified all cortical nodes into seven classes based on the von Economo cytoarchitectonic atlas considering similarities in cell morphologies⁵⁰ (Fig. 2B), which includes the primary sensory (PS), primary motor (PM), primary/secondary sensory (PSS), limbic cortex (LC), default-mode regions (AC1), lateral frontal, parietal, temporal association cortex (AC2) and insular cortex (INS). We calculated the percentage of linear and saturating exponential increases within each class separately and performed chi-square tests between these classes. Compared with primary classes (PS, PM, and PSS), association classes (AC1, AC2, and INS) contained more regions with saturating exponential increases in regional efficiency (Fig. 2B; a matrix

of p values between each pair of classes is given, with red dots representing FDR-corrected $q < 0.05$, corresponding to uncorrected $p = 0.01$). We validated this result with two additional brain partitions: (1) a classic cortical hierarchy classification with four systems⁵¹ and (2) a well-validated cortical functional partition with seven systems⁵². Consistent results were obtained in both validations (Fig. S1).

We then elaborated on the rates of change in regional efficiency along with the development. Figure 2C illustrates the spatial distribution of these rates of change at representative ages. Notably, spatiotemporal changes in regional efficiency were the most pronounced during infancy and were continuously refined in childhood. The regional rates of change in infancy exhibited a hierarchical pattern, as characterized by slow increases in primary cortices such as primary visual and motor areas and rapid increases in transmodal association cortices including the lateral frontal and temporal cortices, medial prefrontal cortex, and insular cortex. To quantify the critical growth phase of each region, we examined age points at which nodal efficiency reached 8/9 of its value at 8 years of age⁷ (Fig. 2D, left panel, white lines). We found that the critical growth phases of transmodal association class (AC1, AC2, and INS) were reached at a median of 4.0 years of age while that of primary class (PM, PS, and PSS) were reached at 7.1 years of age. Next, we calculated the mean rate of change during the critical phase for each node and made a between-class comparison. We found that significantly larger mean rates of change were found in association classes than in primary classes (Fig. 2D, right panel; red dots in the bottom represent the significance of the difference between classes at FDR-corrected $q < 0.05$, corresponding to uncorrected $p = 0.04$ in rank sum tests).

To further investigate whether early developmental rates in regional efficiency predict late childhood network topology, we used support vector regression (SVR) with two-fold cross-validation. Regional rates of change, uniformly sampled at 100 time points between birth and 7.5 years, served as features to predict regional communication efficiency at age 8. To prevent data leakage, the rate of change for each node was estimated while excluding individuals older than 7.5 years. To examine the distinction between primary and association regions, all brain nodes were categorized into these two classes, and predictions were performed separately for each (for details, see “Methods”). We adopted a dual-level significance testing to rigorously evaluate the prediction accuracy during the cross-validation (1000 times). Prediction was considered significant only if it passed: (i) a Pearson correlation test (p_{agg}), in which sample’s prediction values were aggregated across folds and computed a final correlation coefficient with chronological age; and (2) a permutation test (p_{perm}), in which age labels were randomly shuffled across folds to generate a null distribution. We found that predictions were significant only for nodes in the association class (mean $r = 0.34$, $p_{agg} = 0.002$, $p_{perm} < 0.001$, dual-level significance test) but not for those in the primary nodes (mean $r = 0.12$, $p_{agg} = 0.15$, $p_{perm} < 0.001$, dual-level significance test). The r distribution of 1000 random cross validations were shown (Fig. 2E, left panel). Next, to evaluate feature contributions, we conducted another leave-one-out cross-validation (LOOCV) SVR analysis. In this analysis, we used the rates of change in regional efficiency from birth to specific age points as features (Fig. 2E, right panel). We found that the rates of change from birth to ages between 2.7 and 7.5 years were significant predictors ($r = 0.22$ – 0.32 , permutation tests at $p < 0.001$) with the scatter plot depicting the model with the highest accuracy). Notably, the prediction accuracies for the rates of change from birth to age 3 and from birth to age 8 were comparable (0–3 y: $r = 0.28$, representing 92.3% of the maximum r value; Fig. 2E, right panel). These findings underscore the critical role of early postnatal developmental trajectories in shaping the network architecture of late childhood.

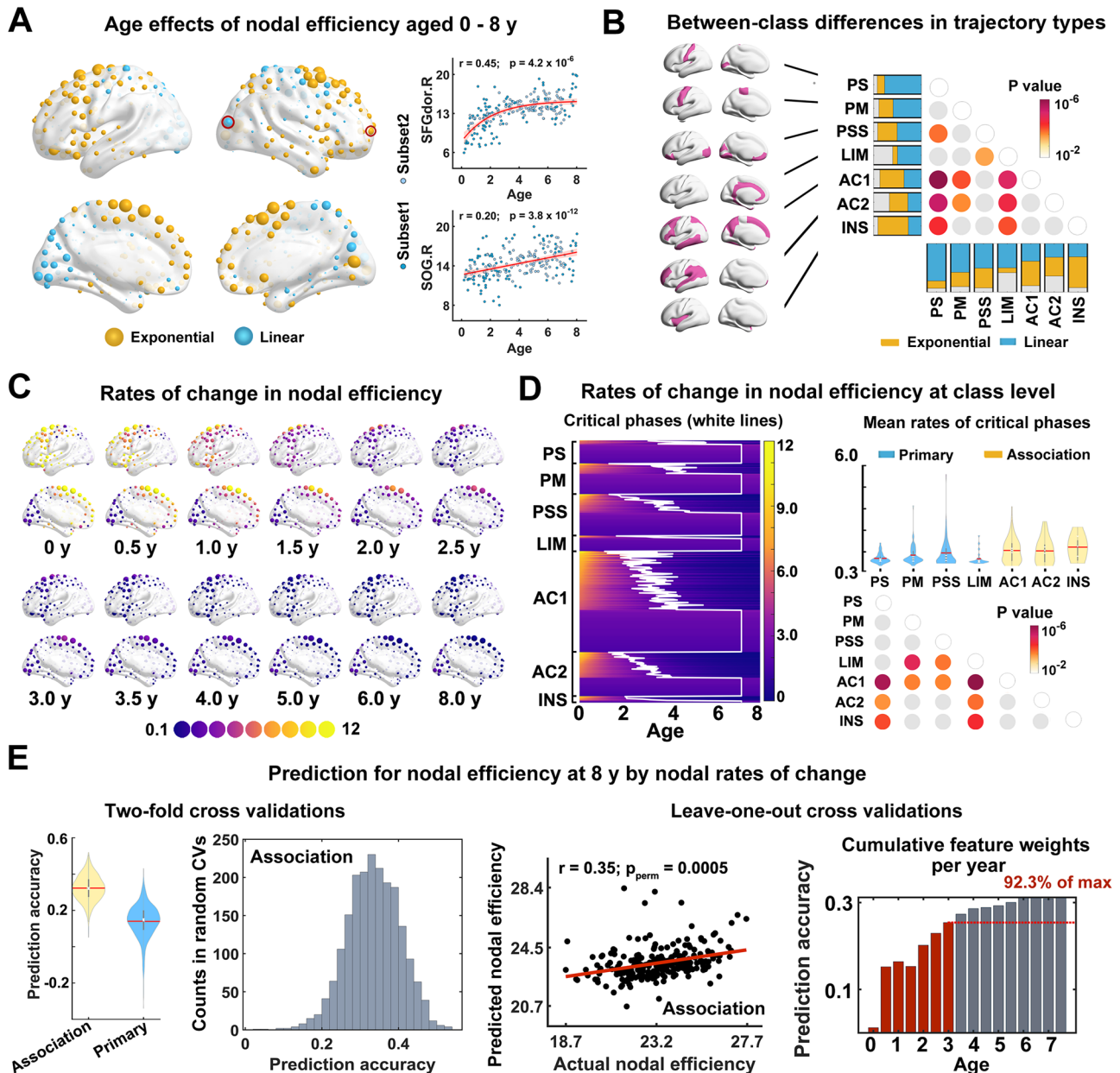


Fig. 2 | Heterogeneous maturation in nodal efficiency of structural brain networks from birth to childhood. **A** Regions showing saturating exponential increases with age (yellow) were found mainly in transmodal association cortex, but linear increases (blue) were found mainly in primary cortex. The scatter plot shows two representative fitting curves (nodes with red circles) with the shaded area indicating the 95% confidence interval around the fitted mean. **B** The group difference in the percentage of saturating exponential increases (exponential: yellow, linear: blue) within seven cortical cytoarchitectonic classes (purple). The p values obtained via chi-square tests are represented as coloured circles (FDR-corrected $q < 0.05$, two tailed). **C** The spatial maps of nodal rates of change at 12 representative age points are plotted. The deep purple to yellow colours represents values from low to high. **D** High rates of change before 3 years of age were identified in association cortex. The regional rates of change along ages are shown in the coloured matrix (deep purple to yellow). The white lines represent critical phases of nodal changes on the basis of age points when nodal efficiency reached 8/9 of its final value (8 y). The violin plots (right panel) represent the distribution of averaged rates of change for the brain nodes within each class (association: yellow, primary: blue). The p values obtained via rank sum tests are shown as coloured circles in the bottom (FDR-corrected $q < 0.05$, two tailed). **E** Model performance in predicting the nodal efficiency at age 8 by regional rates of change at each age point. The network nodes were merged into two classes: one association class ($n = 237$) and one primary class ($n = 173$). SVR prediction analyses were separately performed for

each class with nodal rates of change at each age point as features. Using a two-fold random cross-validation approach, the distribution of prediction capacities was obtained (association: yellow, primary: blue). The prediction for brain nodes in the association class were significant (mean $r = 0.34$, uncorrected $p_{agg} = 0.002$, dual-level significance test, two-tailed), whereas nonsignificant predictions were found for brain nodes in the primary class (mean $r = 0.12$, uncorrected $p_{agg} = 0.15$, dual-level significance test, two-tailed). The violin plots (left panel) represent the distribution of prediction accuracies for the brain nodes within each class. By separately employing a LOOCV prediction strategy for association nodes, we found a maximum prediction accuracy of $r = 0.35$ (right panel). By further breaking features at all age points into age subsegments, we tested the prediction performance in each age range (from 0 y to a certain age point) to reflect the contribution weights of features along with age. Similar prediction accuracies were obtained for the nodal rates of change before age 3 and across the whole 0–8-year age range (before age 3: red colour, 92.3% of max, bottom right panel). For all violin plots, the central white point indicates the median, the red line denotes the mean, black lines represent the interquartile range (25th–75th percentiles), whiskers extend to the most extreme data points within 1.5 \times IQR from the quartiles. PS primary sensory cortex, PM primary motor cortex, PSS primary/secondary sensory cortex, LIM limbic region; AC1 association cortex I, AC2 association cortex II, INS insular cortex, SOG superior occipital gyrus, SFG superior frontal gyrus. Source data are provided as a Source Data file.

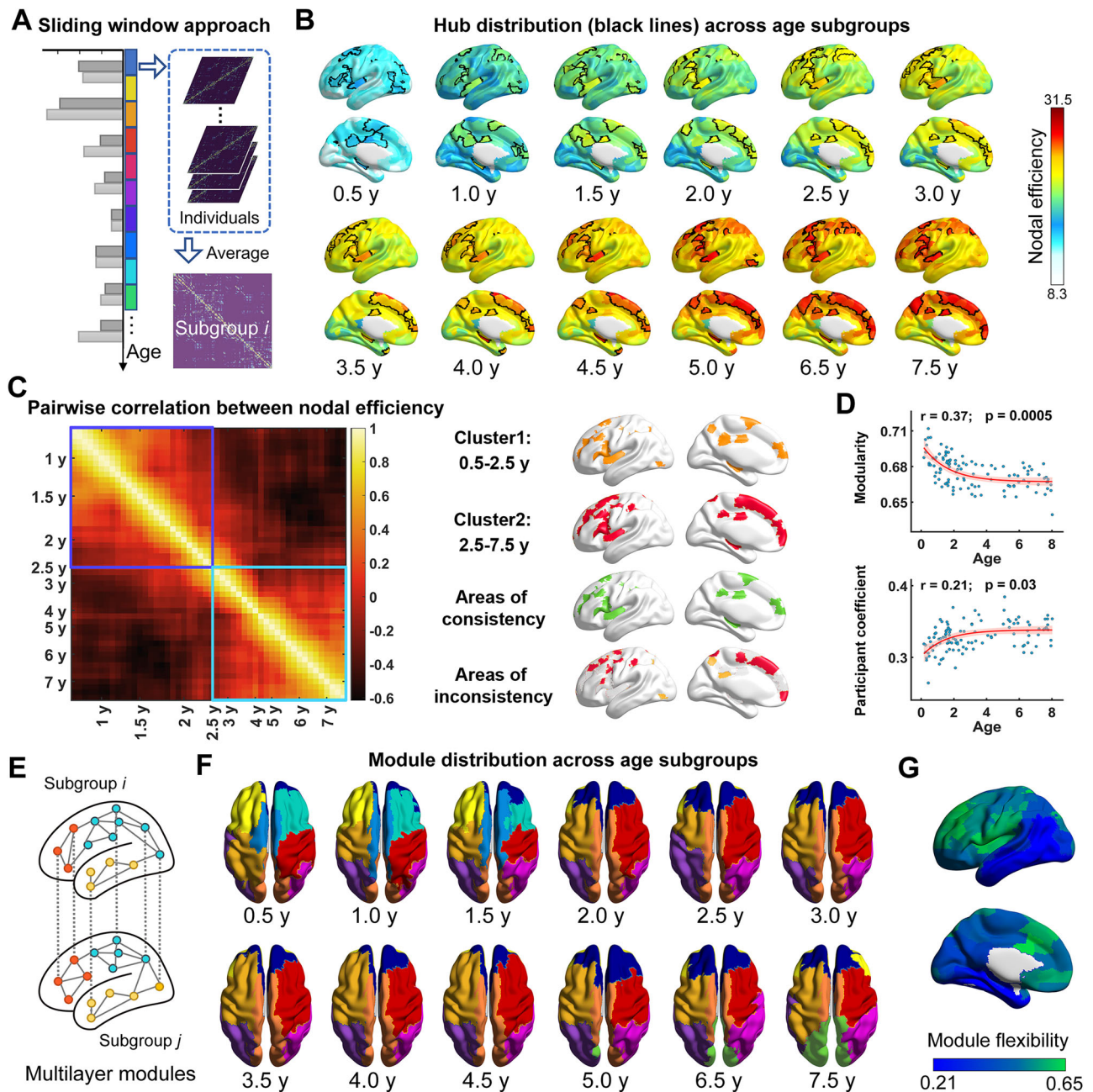


Fig. 3 | Development of the structural hubs and modules from birth to childhood. **A** To delineate the maturation of brain hubs and modules, we used a sliding window approach to generate averaged brain networks and topological metrics at different age points for 100 subgroups. **B** Structural network hubs from birth to age 8 (left hemisphere). The distributions of regional efficiency (white to red) and brain hubs (the top 10% of nodes in terms of nodal efficiency, within black lines) at 12 representative age points ranging from 0.5 years to 7.5 years are shown. For each point, the regional efficiency was averaged across individuals. For detail views, see Fig. S2. **C** A k-means clustering analysis was performed on pairwise correlations (left panel) between nodal efficiency after de-meaning across age subgroups, the best fit was found with two clusters (Fig S3), with an age boundary before and after 2.5 years of age. The distributions of the hub regions in each cluster and the consistent/

inconsistent regions between clusters are plotted (right panel; orange colour: hubs in cluster 1; red colour: hubs in cluster 2; green colour: common hubs in two clusters). **D** Age-related changes (uncorrected p values, two-tailed) in global modularity and the participant coefficient of the brain structural connectome. The scatter plot shows the fitted developmental curves with the shaded area indicating the 95% confidence interval around the fitted mean. **E** A multilayer module detection approach was implemented by an age-ordered conjunction of all averaged matrices in the age subgroups. **F** Cortical module affiliations at 12 representative age points (top view). For detail views, see Fig. S5. **G** High modular flexibility was identified in the frontal association cortex during development (blue to green represent values from low to high). Source data are provided as a Source Data file.

Transmodal association cortices are refined with high hub aggregation and module flexibility

We also investigated the spatiotemporal reconfiguration of network hubs and modular structures during development. Brain hubs represent communication centres in a network, whereas modules capture the extent of a network's division into communities with dense internal links. To

delineate the spatiotemporal maturation of brain hubs, we used a sliding window approach to generate hub maps for 100 age subgroups (Subset 1 of the Discovery Dataset, Fig. 3A). Specifically, we first sorted all the children by age and defined the 15 youngest children as the first subgroup. The remaining 99 subgroups were generated by continuously replacing the youngest child within and outside the

group (without putting back). For each subgroup, we averaged the regional efficiency maps across individuals and defined hubs as the top 10% of nodes in terms of nodal efficiency. Figure 3B shows the distribution of nodal efficiency and identified hubs, which are marked with black lines, at 12 representative ages, ranging from 0.5 years to 7.5 years (for details, see Fig. S2). Notably, we observed that the nodal efficiency already showed spatial heterogeneity even for the neonatal group, in which structural hubs primarily located in the bilateral medial parietal cortex, lateral frontal cortex, insula, middle cingulate cortex, and lateral occipital cortex. Subsequently, structural hubs gradually expand and continue to refine into childhood, particularly in the dorsal medial and lateral prefrontal cortices. To categorize whether these hub maps are clustered into distinct categories across development, we performed k-means clustering on the nodal efficiency maps of all 100 subgroups after demeaning. Silhouette analysis revealed an optimal cluster number of two (Fig. S3), with an age boundary before and after 2.5 years of age (Fig. 3C, left panel). By plotting the typical hub distributions of each cluster, we found that several association regions, including the medial and lateral frontal cortices, cingulate cortex, and insula, were consistently identified as structural hubs from birth to childhood, but there was a clear expansion of hubs in the dorsal parts of the prefrontal cortices (marked in purple) after 2.5 years (Fig. 3C, right panel).

To assess the reconfiguration of network communities during development, we performed a modularity analysis⁵³ for each individual connectome. We found that the global network modularity decreased nonlinearly with age ($r = 0.37$, $p = 0.0005$), whereas the global mean participant coefficient increased nonlinearly with age ($r = 0.21$, $p = 0.03$) (Fig. 3D). These results suggest that the global structural integration between network communities increased progressively during early postnatal development. To elucidate the regional configuration of modular affiliations across development, we further performed a multilayer module detection algorithm (Fig. 3E)⁵³. Briefly, for the 100 age-based subgroups obtained above, we generated 100 group-level matrices by using a consensus approach that preserved the edge length distributions of individual networks⁵⁴. We then connected each subgroup matrix according to its age order to create a multilayer network layout (we set the intralayer resolution as 1 and the interlayer strength as 0.5; for parameter selection details, see SI-2 and Fig. S4). This approach preserves the nonblurred structure of the group modules while accounting for the variation that occurs at each age point. The module partitions at representative age points are shown in Fig. 3F (see Fig. S5 for the module partitions at the other ages). Quantification of the modular variability across subgroups revealed that the modular flexibility was higher in the bilateral prefrontal cortices and insular cortex (Fig. 3G). This result suggests that the reconfiguration of structural hubs in the dorsal prefrontal cortex and insular cortex plays a critical role in inter-module communication from birth to childhood.

Regional topological growths are associated with multiscale neurobiological hierarchies along the sensorimotor-association axis

We demonstrated hierarchical maturation of nodal topology between the association and primary cortices in the structural connectome; thus, we next aimed to assess whether these network changes align with multiscale neurobiological properties along sensorimotor-association (S-A) axes. We included 11 neurobiological maps across the cortex from Sydnor and colleagues²²; these maps are continuous distributions of anatomical hierarchies (cortical myelination, cortical thickness, and externopyramidization), functional hierarchies (the 1st principal component of the functional gradient and neuro-synth), evolutionary hierarchies (macaque-to-human cortical expansion and allometric scaling), energy axes (aerobic glycolysis and cerebral blood flow), and the gene expression axis (the 1st principal component of

brain-expressed genes) and were further aggregated to create an integrated S-A axis. We employed the neuro-map tool⁵⁵ to estimate the spatial correlations between these neurobiological maps and the topological maturation maps. Specifically, spatial association analyses of all 11 maps were performed separately for the mean rates of change (during critical phases) of nodal communication efficiency and nodal module flexibility. The significance of these correlations was estimated via the “spin test” null model, which was used to identify the real spatial similarity rather than spatial autocorrelations. We found that the mean changing rate of nodal efficiency is strongly associated with the integrated S-A axis, anatomical hierarchies, including cortical thickness, cortical myelination and externopyramidization, the evolutionary hierarchy of cortical expansion, the functional hierarchy of PC1 of functional gradient and the gene expression axis (r range: 0.26–0.42; FDR-corrected $q < 0.05$, corresponding to uncorrected $p_{\text{spin}} < 0.005$; Fig. 4A). Nodal module flexibility is significantly associated with the energy metabolism axes, including aerobic glycolysis and cerebral blood flow (r range: 0.28–0.41; FDR-corrected $q < 0.05$, corresponding to uncorrected $p_{\text{spin}} < 0.0003$; Fig. 4B). These results are highly repeatable after controlling for nodal WM microstructural indices as covariates (Tables S1 and 2).

Early rates of change in nodal efficiency shape late childhood network architecture through local WM microstructural maturation

Given that the rates of change in nodal efficiency during early postnatal development predicted network architecture of late childhood (age 8) (Fig. 2E), we examined whether local microstructural maturation of connected WM tracts mediated this relationship²⁹. To address this issue, four diffusion MRI metrics were used to represent WM microstructural properties, including the fractional anisotropy (FA), radial diffusivity (RD), axial diffusivity (AD), and mean diffusivity (MD)^{6,7}. We created the representative map of each metric at each age group by averaging voxel values along node-connected WM tracts and across children within the group. We first focused on the initial and final states of nodal maturation. We estimated the differences in nodal metrics between the primary and association classes, separately for the first and last age groups. Nodal efficiency in the association class was comparable to that of the primary class at birth, but became significantly higher by age 8 (Fig. 5A). Meanwhile, nodal maps of FA, RD, and MD showed a pattern opposite to that of nodal efficiency, with class differences apparent at birth but disappearing by age 8 (the first age group: FA was significantly lower and RD/MD was significantly higher in the association class than those in the primary class, Fig. 5A). These results suggest that the association cortex is initially immature in both white-matter microstructure and network topology at birth. Its subsequent microstructural maturation during early childhood drives a profound topological reorganization, ultimately sculpting it into hub-dense regions with maximal communication capacity by age 8.

Next, we estimated the correlation between the nodal rates of change at each age point and age-8 nodal efficiency. We identified peak correlations between nodal rates of change and age-8 nodal efficiency, which occurred at 3.6 years for association cortex nodes, with no significant effects in primary cortex nodes (Fig. 5B). Last, mediation analyses were then assessed whether local WM microstructure at 3.6 years mediated this developmental link (for details, see “Methods”). Nodal rates of change significantly correlated with nodal FA and RD at 3.6 years of age (Fig. 5C), with both metrics showing full mediation effects (bootstrapped at $p < 0.001$, Fig. 5D). These mediation effects persisted for FA and RD across most developmental stages (Fig. S6). Significant partial mediation effects were also observed for AD or MD (Fig. S6). The findings suggest that early developmental trajectories of association cortices shape maturation of network organization through microstructural development of connected WM pathways, particularly reflected by FA and RD changes. The absence of mediation

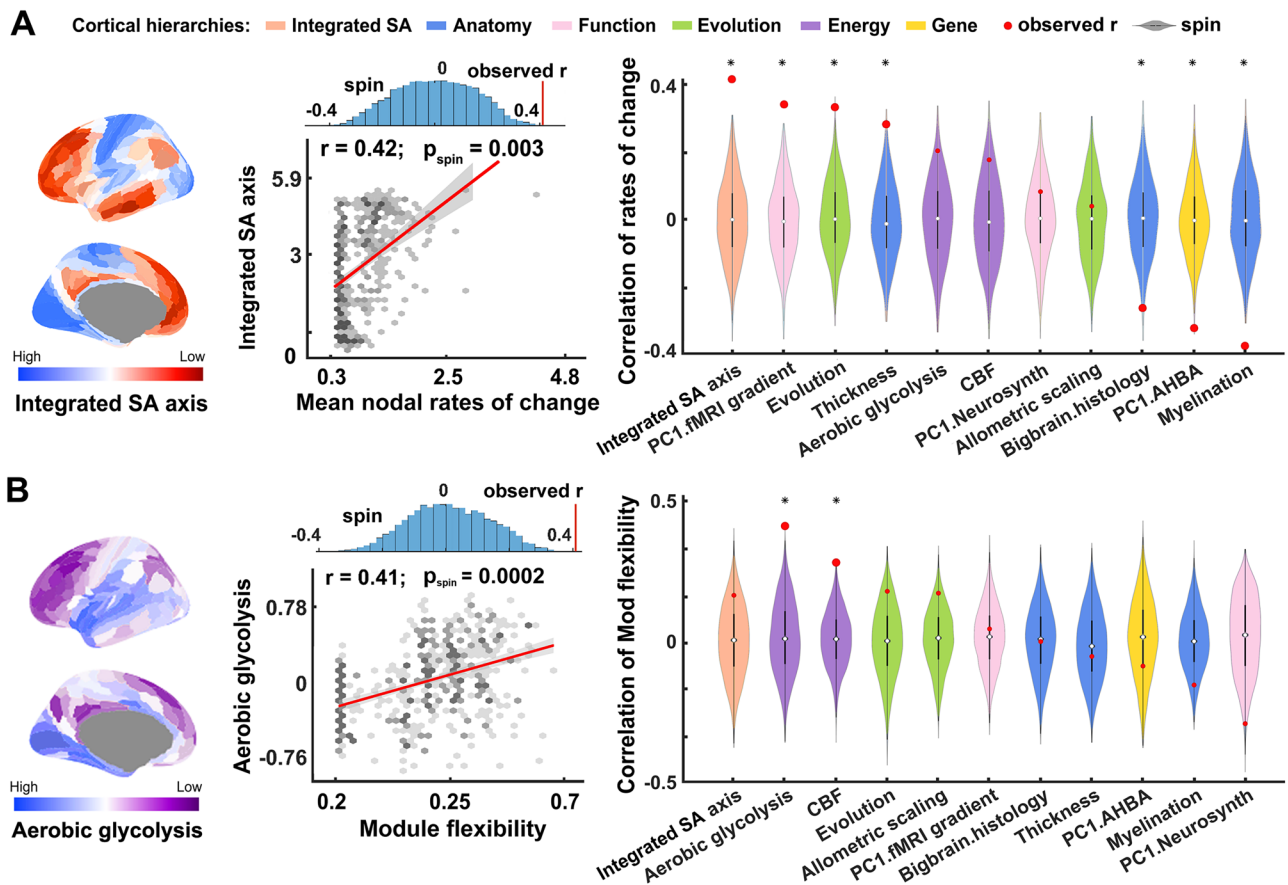


Fig. 4 | Spatial associations between structural network maturation and multiscale neurobiological hierarchies. Eleven neurobiological maps along the sensorimotor-association (S-A) axis were used, including an integrated S-A axis (orange) and 10 detailed axes representing anatomical (blue), functional (pink), evolutionary (green), energy (purple), and gene expression (yellow) hierarchies. By using the neuro-map tool, we estimated the spatial correlations between these maps and maturation maps of nodal topology ($n = 410$), including the mean rates of change in nodal efficiency and the modular flexibility. The significance of the correlations was tested by comparing the real correlation against “spin test” null models after 10,000 permutations. **A** The average rate of change in nodal efficiency is spatially associated with the integrated S-A axis, anatomical hierarchies (cortical thickness, cortical myelination and externopyramidization), the evolutionary hierarchy of cortical expansion, the functional hierarchy of PC1 of functional

gradient and the gene expression axis. **B** Nodal module flexibility is spatially related to energy metabolic hierarchies, including aerobic glycolysis and cerebral blood flow. Left panel: scatter plot shows one of the typical correlations. The shaded area indicates the 95% confidence interval around the fitted mean. (Upper inset: blue bars represent r values from random spin tests (10,000 times), the red line represents the empirical r value); Right panel: the red dots represent observed real correlations. The violin plots represent the null distribution of correlation (“spin test”). The central white point indicates the median, black lines represent the interquartile range (25th–75th percentiles), whiskers extend to the most extreme data points within $1.5 \times \text{IQR}$ from the quartiles. Asterisks represent the significance at FDR-corrected $q < 0.05$ (corresponding to uncorrected $p_{\text{spin}} < 0.005$ and $p_{\text{spin}} < 0.0003$, separately for 4A and 4B, two-tailed). Source data are provided as a Source Data file.

effects in primary nodes aligns with their slow early growths compared to higher-order association regions. This differential mediation pattern underscores the critical role of WM development timing in association cortices in shaping network architecture.

Sensitivity analyses

We evaluated the robustness of our results considering several technical factors, including curve fitting models, cortical parcellation schemes, cross-sample validations, and the effect of head motion (for details, see *SI-4.1 to SI-4.5*). First, to validate the sensitivity of the fitting models on rates of change in nodal efficiency, we replaced the parametric models (linear or saturating exponential model) with a generalized additive model (GAM). This analysis yielded highly convergent results regarding the spatial distribution, prediction power, and neurobiological relevance (Fig. S7). Second, to evaluate the effects of parcellation schemes, we used the AAL-80 structural atlas and Random-500, two different parcellation approaches, to define nodes and performed the same network analysis as those used for the AAL-500 networks. We showed convergent results as shown in the main findings (Fig. S8). Third, to address the impact of sample selection on the fitting

results, we performed two cross-validation strategies: (i) including samples within each site separately (Fig. S9); (ii) employing a five-fold cross-validation (Fig. S10). Finally, we rigorously assessed the impact of head motion on our findings. We quantified the degree of head movement in individual diffusion MRI scans and included these measurements as covariates in the fitting models (Fig. S11). Highly consistent results were obtained in these validation analyses.

To further validate the reproducibility of our findings, we employed two independent cohorts which includes longitudinal scans. The first cohort was from the publicly available BCP dataset⁴⁰, which contains multishell diffusion MRI protocols (processing details are described in *SI-4.6*) before 2.5 years of age under seven diffusion MRI protocols. Following rigorous quality control, we retained 170 brain scans of 98 infants (0–2.5 years) with identical acquisition parameters. The processing pipeline for multi-shell dMRI scans was employed. We observed strong correspondence ($r = 0.71$, $p_{\text{perm}} < 0.0001$) between the averaged structural connectome matrices obtained from age-matched individuals in the two datasets. Subsequent network growth modelling (mixed-effects fitting model) revealed consistent age-dependent alterations in both global network topology and nodal

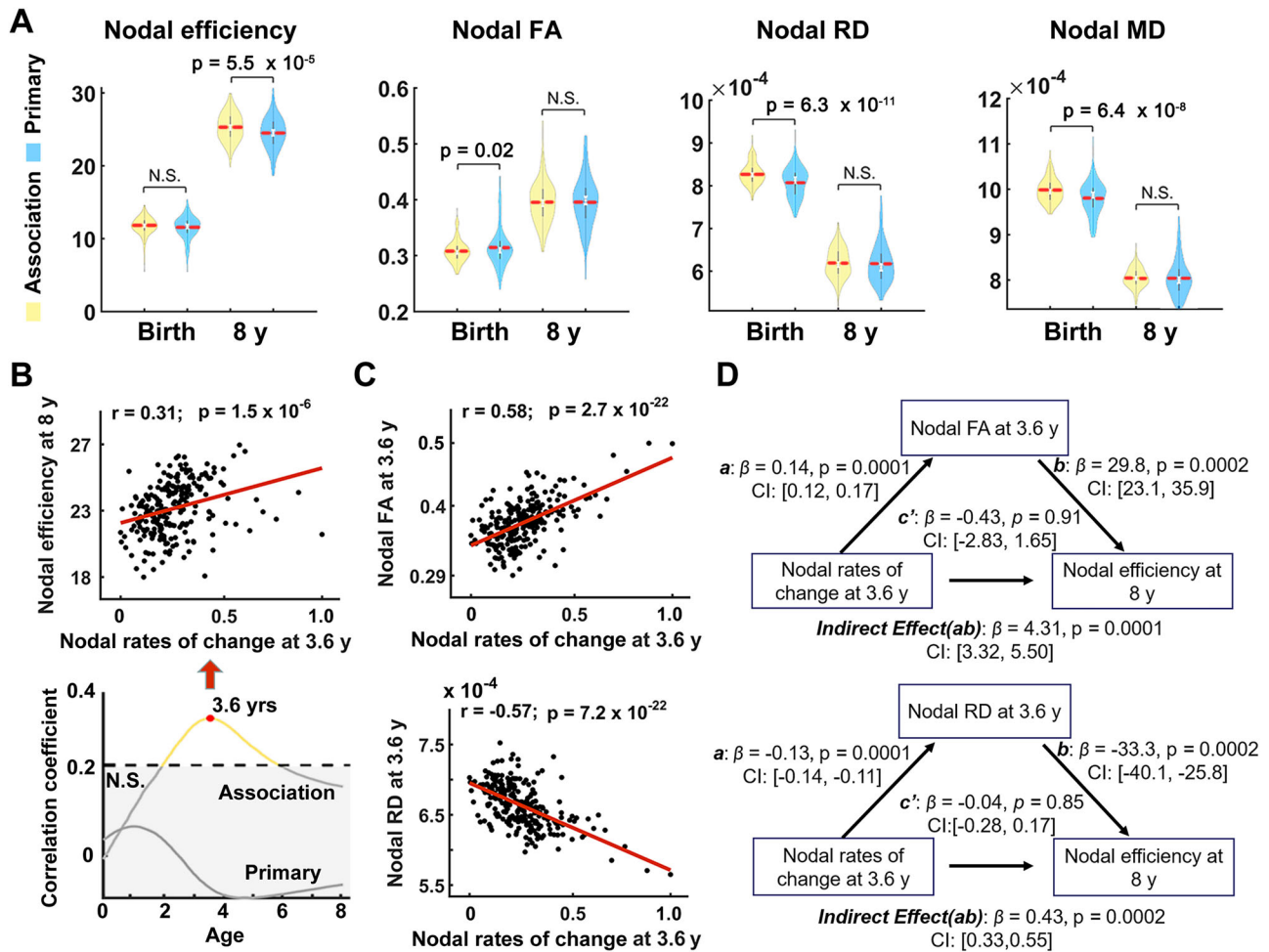


Fig. 5 | The rates of change in nodal efficiency at 3.6 years show the highest correlation with the nodal efficiency at 8 years of age in association cortex, and this relationship is mediated by regional FA and RD metrics. **A** The differences in nodal metrics between the primary and association classes, separately for the first and last age groups ($n = 410$ brain nodes, uncorrected p values, two-tailed). The violin plots represent the distribution of nodal metrics (association: yellow, primary: blue). The central white point indicates the median, the red line denotes the mean, black lines represent the interquartile range (25th–75th percentiles), whiskers extend to the most extreme data points within $1.5 \times$ IQR from the quartiles. **B** The correlation between the nodal rate of change at each age point and the nodal efficiency at 8 years of age (bottom panel, yellow: significant correlations after FDR correction, grey: nonsignificant correlations). The scatter plot for the highest

correlation at 3.6 years of age was given separately (upper panel, two-tailed, uncorrected p values). **C** Significant correlations were observed between rates of change in nodal efficiency and nodal microstructural indices (FA and RD) at 3.6 years of age (uncorrected p values, two-tailed). **D** The significant mediating effect of the nodal FA and RD indices (The significance was determined based on bootstrap confidence intervals). Regional microstructural indices were defined as follows: First, the individual microstructural index maps (separately for the FA, RD, AD and MD metrics) were calculated by averaging the metric values of the voxels along all WM tracts traced from the given nodes. Then, the individual index maps within each age subgroup were averaged as the final regional microstructural representation for each age point. FA fractional anisotropy, RD radial diffusivity, AD axial diffusivity, MD mean diffusivity. Source data are provided as Source Data file.

efficiency metrics (Fig. S12). The second cohort was from the publicly available EBDS dataset⁴¹, which contains single-shell diffusion MRI scans at five age points from 0 to 6 years (0y, 1y, 2y, 4y, 6y). We employed 211 brain scans of 97 infants who underwent at least two follow-up scans. The processing pipeline for single-shell dMRI scans was employed. We observed a major hierarchical maturation pattern of nodal efficiency (Fig. S13). These results confirmed the reproducibility of our findings across independent datasets and processing variations.

Discussion

Our study establishes the hierarchical maturation principles of structural connectomes during infancy and childhood and their neurobiological correlates. We reveal a global network optimization characterized by nonlinear efficiency gains, resilience enhancement, and modular reorganization that occurs predominantly during infancy. Substantial cortex-type divergence emerges between primary

and transmodal association regions through distinct topological trajectories, hub consolidation and module reassignment dynamics, and differential predictive power over late network architecture. These maturation patterns show striking alignment with multiscale biological hierarchies involving anatomy, evolutionary, and energy metabolism. These findings identify biologically constrained critical developmental milestones when connectome reorganization cascades propagate through cortical association systems, ultimately determining the mature network architecture during this critical developmental period.

Accelerated changes in structural network efficiency and robustness from birth to childhood

Previous studies on developments of WM networks have consistently demonstrated age-related increases in global efficiency across different developmental stages in infancy, toddlerhood, and childhood^{28,29,32,34,56}. In our study, we considered the continuous

changes from infancy to childhood, and extended previous findings, revealing nonlinear increases in the topological efficiency of WM networks during development. Such dramatic changes in WM network topology are unlikely to be solely due to overall increases in brain size, as we accounted for brain volume in the statistical models. Moreover, the global efficiency changes nonlinearly, with rapid changes in the initial years followed by slower changes in later years, which is compatible with the maturation of WM microstructures during the same developmental period^{6,7}. The consistency of the maturation curves between the WM microstructure and network efficiency highlights the importance of elucidating the potential link between microstructural integrity and network topology during brain development. We also identified saturating exponential increases in network robustness. While previous studies have shown that brain network robustness gradually increases during development, this robustness remains lower in infants and toddlers than in adults^{29,57}. Particularly, the increased network resilience to hub attacks may suggest a more mature and stable hub configuration that supports centralized processes and ensures reliable neuronal communications. This finding represents a trade-off between network plasticity and stability⁵⁸. These maturation curves of global topological metrics from birth to childhood could serve as potential references for identifying structural connectomic impairments in children with high-risk problems or developmental brain disorders⁵⁹.

Differential topological maturation in the primary and transmodal cortices represents the developmental hierarchy of the structural connectome

The topological refinement of multimodal brain networks during infancy has been widely recognized²⁵. Our findings revealed that the early postnatal developmental changes in nodal topologies of WM networks is well matched with the rooted cortical hierarchies, spanning from primary to association cortices^{51,60}. The early rapid increase of nodal communication efficiency in the transmodal cortex may amplify the difference in information capacity between the primary and association classes, solidifying cortical hierarchies²². This process is further confirmed by the substantial hub reorganization and module reassignment observed in prefrontal cortices and insular cortex. These findings agree with the classic developmental hypothesis of the “orthogenetic principle”, which suggests that general biological development usually progresses from a lack of differentiation to organized differentiation⁶¹. Specifically, the sensorimotor cortex relies on simple feedforward/feedback connections for transient local processing, whereas the transmodal cortex relies on noncanonical parallel connections to support distributed information processing^{51,60,62}. This inherent wiring difference likely contributes to unique topology changes in association cortices during development. Meanwhile, the dramatic topological reorganization in the prefrontal cortex is consistent with prior neuroimaging evidence showing late but rapid myelination of WM microstructures associated with the prefrontal cortex during infancy and early childhood compared with that in other regions^{6,63}. The less mature prefrontal fibre bundles at birth may develop at an accelerated pace to reach the developmental stages of other fibres^{6,19}. This prolonged maturation period may be associated with experience-dependent myelination during infancy and early childhood, which is critical for the gradual forming of high-order cognitive skills (for a review, see ref. 64).

The most notable changes of regional topology during early postnatal development occur in the prefrontal association cortex. While frontal structural hubs are known to emerge in neonate and infancy periods, their connections continue to strengthen throughout childhood and adolescence (for a review, see ref. 25). Of note, we employed a weighted network model and retained the total edge strength, which makes the model more sensitive to changes in hub locations than previous binary and strength-normalized network

models³². Our findings revealed that the unique fast increase in regional efficiency in the dorsal medial frontal region may bring more hub ensembles after ~2.5 years of age. The prolonged prefrontal hubs may facilitate long-range integration among distributed transmodal areas³³, which is crucial for integrated functions such as executive control and abstract conception⁶⁵. The dynamic changes in the topological roles of the frontal cortex observed here are highly consistent with previous lifespan studies of brain WM networks^{53,66} in individuals older than 8 years. Interestingly, Puxeddu and colleagues reported that the medial frontal modules continue to cover both hemispheres into old age⁵³. Future studies leveraging multicentre MRI datasets covering the entire human lifespan will be valuable for fully delineating the forming and refinements of hubs and modules in brain structural networks.

Maturation of regional topological organization is relevant to multiscale neurobiological hierarchies

We found that the rates of change in nodal WM topology from birth to childhood are associated with multiscale cortical hierarchical maps spanning sensorimotor to association cortices, even after controlling for the nodal WM microstructural profiles. The substantial increases in nodal efficiency in the association cortex are accompanied by large evolution expansion and low myelin content. Comparative neuroimaging studies with primates have suggested that the pattern of cortical expansion during development in humans is quite similar to that during evolutionary expansion⁶⁷, marked by nonuniform increases in the frontal cortex⁶⁸. This may reflect the untethering of the human transmodal cortex from canonical sensory–motor circuits⁶⁹. Our findings provide evidence for the close relationship between brain development and evolution from a perspective of topological connectome maturations. Moreover, high module flexibility in the frontal association region is accompanied by high cerebral blood flow⁷⁰ and aerobic glycolysis. At the neuron level, the experience-dependent plasticity of WM networks highly depends on metabolic pathways for sustaining synaptogenesis, long-range axonal elongation, and myelination^{3,4}. Our results indicated that aerobic metabolism may be essential for ensuring flexible adjustments in the topological roles of frontal nodes of the WM network during development. This finding is also consistent with our previous findings that the emergence of brain functional networks⁷¹ is strongly associated with regional cerebral blood flow^{70,72} during early stage. The metabolic requirements of the brain mostly rapidly increase in infancy and peak in childhood^{70,73}. This highlights the necessity of investigating the relationship between energy supply, WM wiring topologies, and brain development diseases⁷⁴. Notably, the low myelination, high expansion, and high energy cost areas in the association cortex are thought to be closely related to the unique intelligence of humans⁷⁵, which indicates that the early wiring patterns of these WM regions may contribute to the later maturation of the unique high-level abilities of humans.

The transitional period from infancy to childhood is highlighted by brain white matter network changes

We identified a critical transitional stage for maturation of the brain structural network, primarily before age 3: the most rapid increases in global efficiency, robustness, and nodal communication efficiency, as well as the most dramatic changes of frontal hubs and modules, all occur during this period. In a separate study involving the same cohort of children, we observed that several microstructural indexes of major WM tracts, quantified by diffusion MRI-derived metrics, changed with the highest rate in infancy period⁷. This critical stage is associated with major milestones in early brain development. A recent study involving 123,984 human brain MRI scans across the entire lifespan presented a normative map of brain WM regions, with the peak WM volume observed at 2.5 years of age¹⁴. Magnetic resonance spectroscopy and positron emission tomography studies have revealed that metabolic

maturation occurs mainly within 3 years of age⁷³. Regional cerebral blood flow also increases dramatically during the first 2 years of life, particularly in the association cortex⁷⁰. Functionally, this key period is characterized by a peak in plasticity⁷⁶, which is critical for coarse-to-fine cognitive development in paediatric patients⁷⁷. These results highlight the importance of identifying potential neuroimaging biomarkers of neuropsychiatric disorders such as autism in this period^{78,79}. It also calls for the need for more detailed brain developmental trajectories before age 3, similar to traditional growth charts for height, weight, and head circumference. This emphasizes the importance of dense sampling in this age range in large-scale brain development projects such as the BCP and the Healthy Brain and Child Development (HBCD) project^{40,80}.

The enhancement of WM microstructure underlies the macro-scale network maturation

The diffusion tensor imaging-based metrics have been widely used to reflect the microstructural changes in WM tracts during development^{6,19}. The increase in FA and decrease in RD are usually thought to be closely related to membrane proliferation and axon myelination^{6,43}. In major association nodes, we observed significant mediating effects of nodal FA and RD on the relationship between rates of change in nodal efficiency and nodal integration capacity at 8 years of age. This finding aligns well with histological evidence that ongoing axonal growth and myelination are the most predominant cellular processes throughout early childhood²¹. Our previous study revealed positive correlations between nodal efficiencies and nodal FA values, as well as inter-tract WM microstructural relevance⁸¹, across three landmark cross-sectional ages from neonates and preadolescents²⁹. Here, we showed that the microstructural properties of WM tracts partly determine how the enhancement in nodal topology at earlier ages contributes to nodal maturation at later ages. This finding suggests that the change of nodal wiring topology is supported by the microstructural enhancement of its connected WM bundles. However, such interpretations should be treated with caution, as image voxels contain massive neurons, and various developmental events can influence diffusion tensor imaging-derived measurements⁹. More advanced diffusion MRI models, such as diffusion kurtosis⁸², multiple tensors⁸³ and neurite orientation dispersion and density imaging⁸⁴, may provide additional information on microstructural changes that better reveal the relationship between WM microstructure and network topology maturation at early ages.

Convergent and divergent functional connectome development relative to structural networks at the critical early stage

fMRI-based studies have delineated the early developmental trajectories of the functional connectome^{9,25,33,85–88}, revealing maturation patterns that are distinct from those observed in the structural connectome. In general, the functional maturation of infant brain lags behind structural maturation. At birth, functional hubs and modules differ markedly from their adult counterparts, being primarily confined to sensory–motor systems^{9,25,33}. During early childhood, these networks undergo pronounced reorganization, following a characteristic transition from local clusters to distributed architecture^{33,89}. By late childhood, major networks establish adult-like functional topography⁹⁰. Accumulating evidence indicates that functional connectome maturation also follows a hierarchical process, with primary systems achieving functional specialization early, whereas association systems develop more gradually over a prolonged course^{87,91}. However, different functional connectome metrics, such as functional specialization, integration, and the organization of positive versus negative connectivity, reveal distinct maturation hierarchies^{85,87}. Recent work suggests that brain functional maturation involves multiple overlapping hierarchical axes rather than a single linear hierarchy⁹². Future multimodal connectome studies combining

structural and functional scans could clarify how the hierarchical maturation of structural wiring scaffolds the emergence of distributed functional networks during the critical 0–8-year window. Such approaches would provide unique insights into how functional architecture arises from structural constraints.

Further considerations

In this study, several issues merit further consideration. First, cross-sectional datasets were employed in this study, which increases the sensitivity of the fitting curves. While we validated our results using longitudinal data from the BCP, these scans covered only the first 2 years of life^{40,80}. Of note, our current design guarantees a relatively even distribution of samples, which benefits normative fitting⁹³. The cross-sectional biases are largely uniform across brain regions, which ensures that comparisons between the primary and transmodal classes are sufficiently fair. Nevertheless, future studies employing multi-centre datasets with large amounts of data and equally distributed longitudinal samples across the entire infancy and childhood are warranted⁴¹. The ongoing HBCD project, which has a longitudinal design, could provide a useful dataset for further validation of our findings⁹⁴. Second, the deterministic tractography was used to construct WM structural networks, thus there was a potential loss of existing fibres⁹⁵. Notably, all currently available tractography algorithms are imperfect in terms of connectome specificity and sensitivity⁹⁶. We validated another probabilistic tractography approach with the primary Subset 2 and BCP dataset which owns a multishell diffusion MRI protocol and reported highly consistent results. Third, the lack of neurodevelopmental outcomes limits elucidation of the relationship between individual brain networks and behavioural development^{12,13}. The creation of large-scale brain and behaviour tracking datasets for the early developmental stage would facilitate such investigations⁹⁴. Finally, future studies with genetic data⁹⁷ will allow the establishment of dynamic associations between brain structural connectome and gene expression profiles during development⁹⁸ and further enable to jointly analyse the relationship between brain network, gene factors, and cognition abilities during development.

Methods

Paediatric participants and data acquisition

The primary dataset comprised two subsets. Subset 1 included 114 typically developing children (50 males and 64 females; mean age: 3.31 ± 2.41 years; age range: 0.17–7.91 years) recruited from Beijing Children's Hospital (Fig. S14). Each child was scanned with a 3T Philips Achieva system (Philips, Best, the Netherlands) under sedation to obtain high-quality diffusion MR (dMRI) images with 30 independent directions at $b = 1000$ s/mm², with two repetitions and 2 mm isotropic resolution, and T1-weighted structural images (T1w) with 1 mm isotropic resolution. These infants were referred to MR imaging due to simple febrile convulsion, convulsion, diarrhea, or sexual precocity. Conducting brain MRIs with sedation in such cases is a routine practice to rule out underlying neurological complications. Sedation was performed after the parents were fully informed and provided consent. Subset 2 included 107 typically developing children (53 males and 54 females; mean age: 4.36 ± 1.78 years; age range: 0.58–7.1 years) recruited from Beijing Normal University (Fig. S14). Each child was scanned with a 3T Siemens PRISMA system at Peking University Third Hospital. High-quality dMRI scans were acquired with 120 independent diffusion-weighted directions across four shells (number of directions = 8, 16, 32, 64, $b = 500, 1000, 2000, 3000$ s/mm²), twelve evenly distributed $b = 0$ scans and two opposite phase-encoding directions (main acquisition: PA, two additional $b = 0$ scans: AP) in 1.7 mm isotropic resolution. T1w images were acquired with 0.8 mm isotropic resolution. These two subsets were separately approved by the Beijing Children's Hospital Research Ethics Committee (approval number

2016-36) and Beijing Normal University Ethics Committee (approval number IRB-A-0002-2022001). The written consent was obtained from the parents of each participating child. The demographic information, exclusion criteria, and data acquisition details are provided in *SI-1*. The replication dataset included two subsets with longitudinal scans (the BCP subset and the EBDs-2 subset), details can be found in *SI-4.6*.

Diffusion MRI preprocessing and network reconstruction

For the single-shell dMRI images (the primary Subset 1 and the replication EBDs-2 subset), image processing included eddy current and small head motion correction, tensor fitting and estimation of diffusion tensor imaging-derived metrics (i.e., FA and diffusivities). The structural network was built with fibres reconstructed from brute-force deterministic tractography⁹⁹ as the network edges and with 500 similar-sized cortical regions subdivided from the AAL atlas as network nodes. We defined the number of streamlines between two regions as the edge weight. For the multi-shell dMRI images (the primary Subset 2 and the replication BCP subset), a different WM connectome reconstruction pipeline was employed. We first used the preprocessing in QSIprep, which included EPI distortion correction, eddy current correction and head motion correction¹⁰⁰. Then, a set of age-specific brain templates¹⁰¹ were employed to warp brain parcellations into individual brain. For fibre reconstruction, we employed the iFOD2 probabilistic tracking algorithm with anatomical constraints (ACT) and estimated streamline weights using the command `tcksift2`¹⁰⁰. A scaling coefficient (μ -factor) was estimated to normalize the total contribution of streamline weights into the FOD-derived fibre density¹⁰². Further details are provided in *SI-2*.

Graph theoretical modelling

Global and regional network metrics were quantified via graph theoretical modelling. For the global metrics, we calculated the global efficiency (E_{glob}), local efficiency (E_{loc}), small-world parameters (λ , γ and σ) and network robustness¹⁰³. For a network graph, the global efficiency measures the parallel information transfer capacity by calculating the average of the reciprocals of the shortest paths. The local efficiency represents how efficient the communication is among the first neighbours. The small-world parameters include three indices. The normalized global efficiency (λ) and normalized local efficiency (γ) measure the ratio between real network efficiency and the mean of that in 100 matched random networks. These two measurements can be summarized into a quantitative metric, small-worldness, $\sigma = \gamma/\lambda$, which is typically greater than 1 for small-world networks^{44,45}. Thus, a small-world network not only has a higher local interconnectivity, but also has an approximately equivalent shortest path length compared with random networks. For network robustness, we assessed how the size of the LCC of the network changed as nodes were progressively removed, either randomly (random failures) or by descending nodal strength (targeted attacks). The robustness was further defined as the area under the resulting LCC–node removal curve, with a larger area indicating greater network resilience.

For the regional metrics, we quantified the regional efficiency, regional hubs and regional module. Notably, the developmental reconfiguration of hubs and modular distribution was quantified using a sliding window design⁵³. Specifically, to prevent site effects, we first sorted 114 children (Subset 1 of the Discovery Dataset) in increasing age order and defined the first 15 children as the first subgroup and the mean age within the subgroup. Next, we generate the remaining 99 subgroups by continuously replacing the youngest child within the group with the child outside the group. Network hubs were defined as the top 10% of nodes in terms of nodal efficiency separately for each age subgroup. A common module affiliation of each node across all age subgroups was identified by a multilayer module detection approach¹⁰⁴. Specifically, we linked each pair of neighbouring age subgroups to create a multilayer network with an intralayer resolution

(γ) of 1 and an interlayer strength (ω) of 0.5. These two parameters were determined by evaluating the balance between sensitivity to age-related changes and module reliability. Then, the heuristic Louvain algorithm¹⁰⁵ was used for the whole multilayer network. Finally, we calculated the modular flexibility of each node by tracking the change in module affiliations over sliding windows for all nodes (More details are provided in *SI-2.4*).

Mapping the developmental curves of the network metrics

To fit the differential growth curves of all network metrics, both linear and saturating exponential models were tested, with sex and brain size included as covariates. We used the AIC¹⁰⁶ and selected the model with the smallest AIC value as the optimal model. The rate of change for a given network metric was defined as the differential coefficient of the optimal fitting curve. We further defined the critical growth phase of each node by identifying the age at which the nodal efficiency reached 8/9 of its final value. The mean rate of change during the critical growth phase was calculated as the representative growth rate of each node. Of note, considering the sensitivity of the fitting models for measuring rates of change in nodal efficiency, we validated the curve fitting with a GAM. Thin plate regression splines were used for the smoothing basis, and the residual estimates of the maximum likelihood method were used to estimate the smoothing parameter. More details are provided in *SI-3.1*.

Predicting regional maturation

SVR with a linear kernel was performed with a two-fold cross-validation (2F–CV) strategy. We set the fitted nodal efficiency at 8 years as the prediction vector ($N_{\text{regions}} \times 1$) and used the rates of change in node efficiency at each age point (uniformly sampled at 100 time points between 0 and 7.5 years) as features (that is, the matrix $N_{\text{regions}} \times N_{\text{age points}}$). To avoid data leakage, we re-estimated the growth curves after removing individuals older than age 7.5. Pearson's correlation coefficient between the predicted values and the observed nodal efficiency of the testing samples was reported as the prediction accuracy. Notably, brain nodes were separated into two classes (association: including AC1, AC2, and INS; and primary: PM, PS, PSS, and LIM), and we performed prediction analyses within each class. We identified the contribution weights by estimating the prediction accuracy of age-specific subfeatures in an additional LOOCV analysis. Further details are provided in *SI-3.2*.

Neuron-map analysis on the relationships between nodal topological maturation and multiscale neurobiological hierarchies

We adopted 11 cortical feature maps which represent diverse fundamental hierarchies of the brain²². These maps include anatomical hierarchies (cortical myelination map, cortical thickness map and externopyramidization), functional hierarchies (functional gradient map and neuro-synth map), evolution-related hierarchies (evolution hierarchy map and allometric scaling map), cerebral metabolism axes (cortical cerebral blood flow map and aerobic glycolysis map), gene expression maps, and integrated sensorimotor–association axis maps. They represent diverse fundamental hierarchies of the brain as continuum patterns rather than as hard classifications and thus include spatial details along the primary and association cortices. The neuron-map tool⁵⁵ was further employed to estimate their spatial correlations with the nodal topological maturation maps by transforming the volume-based features into surface space. The significance levels of these spatial correlations were corrected using “spin test” null models. Further details are provided in *SI-3.4*.

Estimating the mediating effect of WM microstructural properties on the maturation of nodal efficiency

Mediation analyses were performed to investigate whether the relationship between rates of change in nodal efficiency and nodal

integration capacity at 8 years of age was mediated by regional dMRI-derived metrics (FA, RD, AD, and MD) at each age. To obtain regional dMRI measurements, we averaged the voxel metrics along all WM tracts of a given node. We calculated typical regional microstructural metrics across development by averaging the nodal measurements across all individuals within a sliding window subgroup. The significance of the mediator was tested via bootstrapping analysis (10,000 resamples). Further details are provided in SI-3.5.

Reporting summary

Further information on research design is available in the Nature Portfolio Reporting Summary linked to this article.

Data availability

All the data required for reproducing our findings are publicly available, including the individual WM networks, graph theoretical metrics, regional WM microstructural indices, and source data for producing figures. The data are stored in a publicly accessible cloud repository (<https://github.com/tengdazhao/Hierarchical-maturation-WM-connectomes-0-to-8-yrs>). For the primary dataset (subset1 and subset2), raw image scans are available under restricted access. These two datasets belong to an ongoing project that extends into adulthood and includes cognitive assessments alongside multimodal neuroimaging. The principal investigators plan to release the raw data jointly once all data collection is completed. For the Replication Dataset (the BCP subset and the EBDS-2 subset), raw image scans are publicly available at https://nda.nih.gov/edit_collection.html?QA=false&id=2848 and https://nda.nih.gov/edit_collection.html?id=2384, respectively. Source data are provided with this paper.

Code availability

The codes for this study¹⁰⁷ are available on GitHub (<https://github.com/tengdazhao/Hierarchical-maturation-WM-connectomes-0-to-8-yrs>). The software packages used in this manuscript include DTIStudio (<https://www.mristudio.org/>), the Diffusion Toolkit (<http://trackvis.org/>), the SPM8 package (<https://www.fil.ion.ucl.ac.uk/spm/>), FSL v6.0.5 (<https://fsl.fmrib.ox.ac.uk/fsl/fslwiki>), the iBEAT pipeline v2.0 (<https://github.com/iBEAT-V2/iBEAT-V2.0-Docker>), QSIprep v1.0.0.0 (<https://qsiprep.readthedocs.io/en/latest/index.html>), the GRETNA toolbox v2.0.0 (<https://www.nitrc.org/projects/gretna>), the BrainNet Viewer toolbox v 20191031 (<https://www.nitrc.org/projects/bnv>), Support Vector Regression (https://github.com/ZaixuCui/Pattern_Regression_Clean), Neuromaps 0.0.4, <https://github.com/netneurolab/neuromaps>, the Mediation ToolBox (<https://github.com/canlab/MediationToolbox>), R 4.0.3 (<https://www.r-project.org/>), MATLAB 2020b (<https://www.mathworks.com/products/matlab.html>), and Python 3.7.0 (<https://www.python.org/>), which are available online.

References

1. Yakovlev P. I. & Lecours A. R. The myelogenetic cycles of regional maturation of the brain. in *Regional Development of the Brain in Early Life*, 3–70 (Blackwell Scientific Publications, 1967).
2. Silbereis, J. C., Pochareddy, S., Zhu, Y., Li, M. & Sestan, N. The cellular and molecular landscapes of the developing human central nervous system. *Neuron* **89**, 248–268 (2016).
3. Steiner, P. Brain fuel utilization in the developing brain. *Ann. Nutr. Metabol.* **75**, 8–18 (2019).
4. Hirrlinger, J. & Nave, K. A. Adapting brain metabolism to myelination and long-range signal transduction. *Glia* **62**, 1749–1761 (2014).
5. Grotheer, M. et al. White matter myelination during early infancy is linked to spatial gradients and myelin content at birth. *Nat. Commun.* **13**, 997 (2022).
6. Ouyang, M., Dubois, J., Yu, Q., Mukherjee, P. & Huang, H. Delimitation of early brain development from fetuses to infants with diffusion MRI and beyond. *NeuroImage* **185**, 836–850 (2019).
7. Yu, Q. et al. Differential white matter maturation from birth to 8 years of age. *Cereb. Cortex* **30**, 2674–2690 (2020).
8. Feng, L. et al. Age-specific gray and white matter DTI atlas for human brain at 33, 36 and 39 postmenstrual weeks. *NeuroImage* **185**, 685–698 (2019).
9. Zhao, T., Xu, Y. & He, Y. Graph theoretical modeling of baby brain networks. *NeuroImage* **185**, 711–727 (2019).
10. Nagy, Z., Westerberg, H. & Klingberg, T. Maturation of white matter is associated with the development of cognitive functions during childhood. *J. Cogn. Neurosci.* **16**, 1227–1233 (2004).
11. Girault, J. B. et al. White matter connectomes at birth accurately predict cognitive abilities at age 2. *NeuroImage* **192**, 145–155 (2019).
12. Ball, G. et al. Thalamocortical connectivity predicts cognition in children born preterm. *Cereb. Cortex* **25**, 4310–4318 (2015).
13. Ouyang, M. et al. Diffusion-MRI-based regional cortical microstructure at birth for predicting neurodevelopmental outcomes of 2-year-olds. *eLife* **9**, e58116 (2020).
14. Bethlehem, R. A. I. et al. Brain charts for the human lifespan. *Nature* **604**, 525–533 (2022).
15. Lim, L., Mi, D., Llorca, A. & Marin, O. Development and functional diversification of cortical interneurons. *Neuron* **100**, 294–313 (2018).
16. Tau, G. Z. & Peterson, B. S. Normal development of brain circuits. *Neuropsychopharmacology* **35**, 147–168 (2010).
17. Sydnor, V. J. et al. Intrinsic activity development unfolds along a sensorimotor–association cortical axis in youth. *Nat. Neurosci.* **26**, 638–649 (2023).
18. Dubois, J. et al. The early development of brain white matter: a review of imaging studies in fetuses, newborns and infants. *Neuroscience* **276**, 48–71 (2014).
19. Huang, H. Imaging the infant brain. in *Oxford Research Encyclopedia of Psychology* (Oxford University Press, 2022).
20. Guillery, R. Is postnatal neocortical maturation hierarchical? *Trends Neurosci.* **28**, 512–517 (2005).
21. Huttenlocher, P. R. & Dabholkar, A. S. Regional differences in synaptogenesis in human cerebral cortex. *J. Comp. Neurol.* **387**, 167–178 (1997).
22. Sydnor, V. J. et al. Neurodevelopment of the association cortices: patterns, mechanisms, and implications for psychopathology. *Neuron* **109**, 2820–2846 (2021).
23. Stephens, R. L. et al. White matter development from birth to 6 years of age: a longitudinal study. *Cereb. Cortex* **30**, 6152–6168 (2020).
24. Huang, H. et al. White and gray matter development in human fetal, newborn and pediatric brains. *NeuroImage* **33**, 27–38 (2006).
25. Cao, M., Huang, H. & He, Y. Developmental connectomics from infancy through early childhood. *Trends Neurosci.* **40**, 494–506 (2017).
26. Brown, C. J. et al. Structural network analysis of brain development in young preterm neonates. *NeuroImage* **101**, 667–680 (2014).
27. van den Heuvel, M. P. et al. The neonatal connectome during preterm brain development. *Cereb. Cortex* **25**, 3000–3013 (2015).
28. Zhao, T. et al. Structural network maturation of the preterm human brain. *NeuroImage* **185**, 699–710 (2019).
29. Huang, H. et al. Development of human brain structural networks through infancy and childhood. *Cereb. Cortex* **25**, 1389–1404 (2015).

30. Hagmann, P. et al. White matter maturation reshapes structural connectivity in the late developing human brain. *Proc. Natl. Acad. Sci. USA* **107**, 19067–19072 (2010).
31. Tymofiyeva, O. et al. Towards the baby connectome: mapping the structural connectivity of the newborn brain. *PLoS ONE* **7**, e31029 (2012).
32. Bagonis, M. et al. Early childhood development of node centrality in the white matter connectome and its relationship to IQ at age 6 years. *Biol. Psychiatry. Cogn. Neurosci. Neuroimaging* **8**, 1024–1032 (2023).
33. Oldham, S., Ball, G. & Fornito, A. Early and late development of hub connectivity in the human brain. *Curr. Opin. Psychol.* **44**, 321–329 (2022).
34. Yap, P. T. et al. Development trends of white matter connectivity in the first years of life. *PLoS ONE* **6**, e24678 (2011).
35. Keunen, K., Counsell, S. J. & Benders, M. The emergence of functional architecture during early brain development. *NeuroImage* **160**, 2–14 (2017).
36. Ball, G. et al. Rich-club organization of the newborn human brain. *Proc. Natl. Acad. Sci. USA* **111**, 7456–7461 (2014).
37. Baum, G. L. et al. Modular segregation of structural brain networks supports the development of executive function in youth. *Curr. Biol.* **27**, 1561–1572 e1568 (2017).
38. Bagautdinova, J. et al. Development of white matter fiber covariance networks supports executive function in youth. *Cell Rep.* **42**, 113487 (2023).
39. Gilmore, J. H., Knickmeyer, R. C. & Gao, W. Imaging structural and functional brain development in early childhood. *Nat. Rev. Neurosci.* **19**, 123–137 (2018).
40. Howell, B. R. et al. The UNC/UMN Baby Connectome Project (BCP): an overview of the study design and protocol development. *NeuroImage* **185**, 891–905 (2019).
41. Alex, A. M. et al. A global multicohort study to map subcortical brain development and cognition in infancy and early childhood. *Nat. Neurosci.* **27**, 176–186 (2024).
42. Craddock, R. C. et al. Imaging human connectomes at the macroscale. *Nat. Methods* **10**, 524–539 (2013).
43. Lebel, C., Treit, S. & Beaulieu, C. A review of diffusion MRI of typical white matter development from early childhood to young adulthood. *NMR Biomed.* **32**, e3778 (2019).
44. Maslov, S. & Sneppen, K. Specificity and stability in topology of protein networks. *Science* **296**, 910–913 (2002).
45. Latora, V. & Marchiori, M. Efficient behavior of small-world networks. *Phys. Rev. Lett.* **87**, 198701 (2001).
46. Humphries, M. D., Gurney, K. & Prescott, T. J. The brainstem reticular formation is a small-world, not scale-free, network. *Proc. R. Soc. B Biol. Sci.* **273**, 503–511 (2006).
47. Watts, D. J. & Strogatz, S. H. Collective dynamics of small-world networks. *Nature* **393**, 440–442 (1998).
48. Achard, S., Salvador, R., Whitcher, B., Suckling, J. & Bullmore, E. A resilient, low-frequency, small-world human brain functional network with highly connected association cortical hubs. *J. Neurosci.* **26**, 63–72 (2006).
49. Albert, R., Jeong, H. & Barabasi, A. L. Error and attack tolerance of complex networks. *Nature* **406**, 378–382 (2000).
50. von Economo, C. F. & GNK. *Die Cytoarchitektonik der Hirnrinde des Erwachsenen Menschen* (Springer, 1925).
51. Mesulam, M. M. From sensation to cognition. *Brain* **121**, 1013–1052 (1998).
52. Yeo, B. T. et al. The organization of the human cerebral cortex estimated by intrinsic functional connectivity. *J. Neurophysiol.* **106**, 1125–1165 (2011).
53. Puxeddu, M. G. et al. The modular organization of brain cortical connectivity across the human lifespan. *NeuroImage* **218**, 116974 (2020).
54. Betzel, R. F. & Bassett, D. S. Specificity and robustness of long-distance connections in weighted, interareal connectomes. *Proc. Natl. Acad. Sci. USA* **115**, E4880–E4889 (2018).
55. Markello, R. D. et al. neuromaps: structural and functional interpretation of brain maps. *Nat. Methods* **19**, 1472–1479 (2022).
56. Batalle, D. et al. Early development of structural networks and the impact of prematurity on brain connectivity. *NeuroImage* **149**, 379–392 (2017).
57. Gao, W. et al. Temporal and spatial evolution of brain network topology during the first two years of life. *PLoS ONE* **6**, e25278 (2011).
58. Vogel, G. *Can we Make our Brains More Plastic?* (American Association for the Advancement of Science, 2012).
59. Ouyang, M. et al. Flattened structural network changes and association of hyperconnectivity with symptom severity in 2–7-year-old children with autism. *Front. Neurosci.* **15**, 757838 (2022).
60. Huntenburg, J. M., Bazin, P.-L. & Margulies, D. S. Large-scale gradients in human cortical organization. *Trends Cogn. Sci.* **22**, 21–31 (2018).
61. Sameroff, A. A unified theory of development: a dialectic integration of nature and nurture. *Child Dev.* **81**, 6–22 (2010).
62. Margulies, D. S. et al. Situating the default-mode network along a principal gradient of macroscale cortical organization. *Proc. Natl. Acad. Sci. USA* **113**, 12574–12579 (2016).
63. Deoni, S. C. et al. Investigating white matter development in infancy and early childhood using myelin water fraction and relaxation time mapping. *NeuroImage* **63**, 1038–1053 (2012).
64. Hodel, A. S. Rapid infant prefrontal cortex development and sensitivity to early environmental experience. *Dev. Rev.* **48**, 113–144 (2018).
65. Shaffer, D. R. & Kipp, K. *Developmental Psychology Childhood and Adolescence* 8th edn (Belmont: Wadsworth, 2009).
66. Zhao, T. et al. Age-related changes in the topological organization of the white matter structural connectome across the human lifespan. *Hum. Brain Mapp.* **36**, 3777–3792 (2015).
67. Hill, J. et al. Similar patterns of cortical expansion during human development and evolution. *Proc. Natl. Acad. Sci. USA* **107**, 13135–13140 (2010).
68. Rilling, J. K. Comparative primate neuroimaging: insights into human brain evolution. *Trends Cogn. Sci.* **18**, 46–55 (2014).
69. Buckner, R. L. & Krienen, F. M. The evolution of distributed association networks in the human brain. *Trends Cogn. Sci.* **17**, 648–665 (2013).
70. Ouyang, M. et al. Spatiotemporal cerebral blood flow dynamics underlies emergence of the limbic-sensorimotor-association cortical gradient in human infancy. *Nat. Commun.* **15**, 8944 (2024).
71. Cao, M. et al. Early development of functional network segregation revealed by connectomic analysis of the preterm human brain. *Cereb. Cortex* **27**, 1949–1963 (2017).
72. Yu, Q. et al. Infant brain regional cerebral blood flow increases supporting emergence of the default-mode network. *eLife* **12**, e78397 (2023).
73. Kuzawa, C. W. et al. Metabolic costs and evolutionary implications of human brain development. *Proc. Natl. Acad. Sci. USA* **111**, 13010–13015 (2014).
74. Morella I. M., Brambilla R. & Morè L. Emerging roles of brain metabolism in cognitive impairment and neuropsychiatric disorders. *Neurosci. Biobehav. Rev.* **142**, 104892 (2022).
75. Fjell, A. M. et al. High-expanding cortical regions in human development and evolution are related to higher intellectual abilities. *Cereb. Cortex* **25**, 26–34 (2015).
76. Qiu, A., Mori, S. & Miller, M. I. Diffusion tensor imaging for understanding brain development in early life. *Annu. Rev. Psychol.* **66**, 853–876 (2015).

77. Dosman, C. F., Andrews, D. & Goulden, K. J. Evidence-based milestone ages as a framework for developmental surveillance. *Paediatr. Child Health* **17**, 561–568 (2012).
78. Cao, M., Huang, H., Peng, Y., Dong, Q. & He, Y. Toward developmental connectomics of the human brain. *Front. Neuroanat.* **10**, 25 (2016).
79. Marin, O. Developmental timing and critical windows for the treatment of psychiatric disorders. *Nat. Med.* **22**, 1229–1238 (2016).
80. Volkow, N. D. et al. An examination of child and adolescent neurodevelopment through National Institutes of Health Studies. *Public Health Rep.* **135**, 169–172 (2020).
81. Mishra, V. et al. Differences of inter-tract correlations between neonates and children around puberty: a study based on microstructural measurements with DTI. *Front. Hum. Neurosci.* **7**, 721 (2013).
82. Ouyang, M. et al. Differential cortical microstructural maturation in the preterm human brain with diffusion kurtosis and tensor imaging. *Proc. Natl. Acad. Sci. USA* **116**, 4681–4688 (2019).
83. Mishra, V., Guo, X., Delgado, M. R. & Huang, H. Toward tract-specific fractional anisotropy (TSFA) at crossing-fiber regions with clinical diffusion MRI. *Magn. Reson. Med.* **74**, 1768–1779 (2015).
84. Zhang, H., Schneider, T., Wheeler-Kingshott, C. A. & Alexander, D. C. NODDI: practical in vivo neurite orientation dispersion and density imaging of the human brain. *NeuroImage* **61**, 1000–1016 (2012).
85. Li, Q. et al. Development of segregation and integration of functional connectomes during the first 1000 days. *Cell Rep.* **43**, 114168 (2024).
86. Hong, Y. et al. Structural and functional connectome relationships in early childhood. *Dev. Cogn. Neurosci.* **64**, 101314 (2023).
87. Yin, W. et al. Charting brain functional development from birth to 6 years of age. *Nat. Hum. Behav.* **9**, 1246–1259 (2025).
88. Zhang, H., Shen, D. & Lin, W. Resting-state functional MRI studies on infant brains: a decade of gap-filling efforts. *NeuroImage* **185**, 664–684 (2019).
89. Sun, L. et al. Human lifespan changes in the brain's functional connectome. *Nat. Neurosci.* **28**, 891–901 (2025).
90. Tooley, U. A., Bassett, D. S. & Mackey, A. P. Functional brain network community structure in childhood: Unfinished territories and fuzzy boundaries. *NeuroImage* **247**, 118843 (2022).
91. França, L. G. et al. Neonatal brain dynamic functional connectivity in term and preterm infants and its association with early childhood neurodevelopment. *Nat. Commun.* **15**, 16 (2024).
92. Gao, W. A hierarchical model of early brain functional network development. *Trends Cogn. Sci.* **29**, 855–868 (2025).
93. Kang, K. et al. Study design features increase replicability in brain-wide association studies. *Nature* **636**, 719–727 (2024).
94. Jordan, C. J., Weiss, S. R., Howlett, K. D. & Freund, M. P. Introduction to the special issue on Informing longitudinal studies on the effects of maternal stress and substance use on child development: planning for the HEALTHY brain and child development (HBCD) study. *Advers. Resil. Sci.* **1**, 217–221 (2020).
95. Maier-Hein, K. H. et al. The challenge of mapping the human connectome based on diffusion tractography. *Nat. Commun.* **8**, 1–13 (2017).
96. Zalesky, A. et al. Connectome sensitivity or specificity: which is more important? *NeuroImage* **142**, 407–420 (2016).
97. Zhao, B. et al. Common genetic variation influencing human white matter microstructure. *Science* **372**, eabf3736 (2021).
98. Liang, X. et al. Structural connectome architecture shapes the maturation of cortical morphology from childhood to adolescence. *Nat. Commun.* **15**, 784 (2024).
99. Huang, H., Zhang, J., van Zijl, P. & Mori, S. Analysis of noise effects on DTI-based tractography using the brute-force and multi-ROI approach. *Magn. Reson. Med.* **52**, 559–565 (2004).
100. Cieslak, M. et al. QSIprep: an integrative platform for preprocessing and reconstructing diffusion MRI data. *Nat. Methods* **18**, 775–778 (2021).
101. Chen, L. et al. A 4D infant brain volumetric atlas based on the UNC/UMN baby connectome project (BCP) cohort. *NeuroImage* **253**, 119097 (2022).
102. Smith, R. E., Raffelt, D., Tournier, J.-D. & Connelly, A. Quantitative streamlines tractography: methods and inter-subject normalisation. *Aperture Neuro* **2**, 1–25 (2022).
103. Rubinov, M. & Sporns, O. Complex network measures of brain connectivity: uses and interpretations. *NeuroImage* **52**, 1059–1069 (2010).
104. Mucha, P. J., Richardson, T., Macon, K., Porter, M. A. & Onnela, J.-P. Community structure in time-dependent, multiscale, and multiplex networks. *Science* **328**, 876–878 (2010).
105. Blondel V. D., Guillaume J.-L., Lambiotte R. & Lefebvre E. Fast unfolding of communities in large networks. *J. Stat. Mech. Theory Exp.* **2008**, P10008 (2008).
106. Akaike, H. A new look at statistical-model identification. *IEEE Trans. Autom. Control* **19**, 716–723 (1974).
107. Zhao, T. et al. Hierarchical maturation of structural brain connectomes from birth to childhood. Zenodo <https://doi.org/10.5281/zenodo.18039533> (2025).

Acknowledgements

The study was supported by the National Natural Science Foundation of China (Nos. 82021004 (Y.H.), 31830034 (Y.H.), 12171330 (Y.P.), 82302287 (R.H.)), the STI 2030-Major Projects of Brain Science and Brain-Inspired Intelligence Technology (No. 2021ZD0200508 (Y.P.)), the Fundamental Research Funds for the Central Universities (Nos. 2233300002 (T.Z.), 2233100018 (T.Z.)), and the National Institute of Health (Grant Nos. R01MH092535 (H. H.), R01MH125333 (H. H.), R01EB031284 (H. H.), R01MH129981 (H. H.), R21MH123930 (M. O.), and P50HD105354 (H. H.)).

Author contributions

T.Z., M.O., H.H., and Y.H. designed the research; Y.P., X.S., D.H., H.K., J.G., Y.L., H.Y., R.H., Q.W., and M.L. collected the imaging dataset; T.Z. performed the research; M.O., X.L., S.Z., M.H., J.J., L.S., X.W., and Y.X. provided technical assistance; T.Z. wrote the paper; and T.Z., M.O., H.H., and Y.H. revised the paper.

Competing interests

The authors declare no competing interests.

Additional information

Supplementary information The online version contains supplementary material available at <https://doi.org/10.1038/s41467-026-68704-w>.

Correspondence and requests for materials should be addressed to Yun Peng, Hao Huang or Yong He.

Peer review information *Nature Communications* thanks Gareth Ball and the other, anonymous, reviewer(s) for their contribution to the peer review of this work. A peer review file is available.

Reprints and permissions information is available at <http://www.nature.com/reprints>

Publisher's note Springer Nature remains neutral with regard to jurisdictional claims in published maps and institutional affiliations.

Open Access This article is licensed under a Creative Commons Attribution-NonCommercial-NoDerivatives 4.0 International License, which permits any non-commercial use, sharing, distribution and reproduction in any medium or format, as long as you give appropriate credit to the original author(s) and the source, provide a link to the Creative Commons licence, and indicate if you modified the licensed material. You do not have permission under this licence to share adapted material derived from this article or parts of it. The images or other third party material in this article are included in the article's Creative Commons licence, unless indicated otherwise in a credit line to the material. If material is not included in the article's Creative Commons licence and your intended use is not permitted by statutory regulation or exceeds the permitted use, you will need to obtain permission directly from the copyright holder. To view a copy of this licence, visit <http://creativecommons.org/licenses/by-nc-nd/4.0/>.

© The Author(s) 2026